Timescale of overturn in a magma ocean cumulate

A. Morison, S. Labrosse, R. Deguen, T. Alboussière

Timescale of overturn in a magma ocean cumulate

A. Morison[a,*], S. Labrosse[a], R. Deguen[a], T. Alboussière[a]

[a] *Université de Lyon, ENSL, UCBL, CNRS, LGL-TPE, 46 allée d'Italie, F-69364 Lyon, France*

Abstract

The formation and differentiation of planetary bodies are thought to involve magma oceans stages. We study the case of a planetary mantle crystallizing upwards from a global magma ocean. In this scenario, it is often considered that the magma ocean crystallizes more rapidly than the time required for convection to develop in the solid cumulate. This assumption is appealing since the temperature and composition profiles resulting from the crystallization of the magma ocean can be used as an initial condition for convection in the solid part. We test here this assumption with a linear stability analysis of the density profile in the solid cumulate as crystallization proceeds. The interface between the magma ocean and the solid is a phase change interface. Convecting matter arriving near the interface can therefore cross this boundary via melting or freezing. We use a semi-permeable condition at the boundary between the magma ocean and the solid to account for that phenomenon. The timescale with which convection develops in the solid is found to be several orders of magnitude smaller than the time needed to crystallize the magma ocean as soon as a few hundreds kilometers of cumulate are formed on a Mars- to Earth-size planet. The phase change boundary condition is found to decrease this timescale by several orders of magnitude. For a Moon-size object, the possibility of melting and freezing at the top of the cumulate allows the overturn to happen before complete crystallization. The convective patterns are also affected by melting and freezing at the boundary: the linearly most-unstable mode is a degree-1 translation mode instead of the approximately aspect-ratio-one convection rolls found with classical non-penetrative boundary conditions. The first overturn of the crystallizing cumulate on Mars and the Moon could therefore be at the origin of their observed degree-1 features.

Keywords: magma ocean, overturn, mantle dynamics, linear stability

1. Introduction

A common scenario considered for the formation of terrestrial planets is the crystallization of a global magma ocean from the bottom-up, because the liq-

*Corresponding author adrien.morison@ens-lyon.fr

uidus of silicate magmas increases with pressure more steeply than the isentropic temperature, at least at low to moderate mantle pressure (Andrault et al., 2011; Fiquet et al., 2010; Thomas and Asimow, 2013; Boukaré et al., 2015). The crystallization of the surface magma ocean is expected to be rapid, around 1 Myr (e.g. Abe, 1997; Lebrun et al., 2013). This has led several authors to assume convection in the solid part of the crystallizing mantle does not start until the mantle is entirely crystallized (e.g. Hess and Parmentier, 1995; Abe, 1997; Parmentier et al., 2002; Elkins-Tanton et al., 2003, 2005; Zhang et al., 2013). However, this assumption deserves scrutiny since the compositional and thermal structure of the mantle after complete crystallization could be widely different if solid-state convection does set in during its crystallization.

Two processes might lead to the destabilization of the solid mantle during its crystallization. First, assumming fractional crystallization, the surface magma ocean gets enriched in incompatible elements. As a secondary result, the new solid formed at the solid/liquid boundary gets richer and richer in these elements as crystallization progresses. Iron is such an element and its abundance is such that it affects significantly the density of both the solid and the liquid. The solid formed at the end of the crystallization is richer in iron than the solid formed at the beginning of the crystallization, leading to an unstable setup with material denser at the top than at the bottom of the solid mantle.

The second process that can further destabilize the solid mantle is the temperature gradient in the solid. The solidus temperature increases with pressure, and is steeper than the isentropic temperature profile. Assuming the temperature in the solid stays close to the solidus, the resulting profile is hence unstable. This effect is enhanced by fractional crystallization and the associated enrichment of the solid in incompatible elements: their presence further decreases the solidus temperature and the compositional gradient discussed above induces an even steeper solidus.

Numerical simulations including these processes suggest it is possible for solid-state convection to set in prior to the entire crystallization of the surface magma ocean (e.g. Maurice et al., 2017; Boukaré et al., 2018). Whether convection in the mantle starts during or after the crystallization of the surface magma ocean is found to have profound implications on the preservation of compositional heterogeneities as well as the dynamics of the mantle (Ballmer et al., 2017; Tosi et al., 2013). These results further confirm the need to assess the parameters controlling the onset of convection in the primitive mantle.

A dynamical feature of the solid cumulate in contact with a magma ocean that has not been accounted for in the past studies is the possibility of exchange of matter at the boundary between the solid and the ocean via melting and freezing. We use a boundary condition developed for the inner core boundary (Deguen et al., 2013) to take this effect into account. This boundary condition is expected to have important effects on the convection pattern and heat flux as well as the timescale with which convection sets in (Deguen, 2013; Labrosse et al., 2018).

Our aim is to assess how the timescale at which convection starts in the solid cumulate compares with the time needed to crystallize a surface magma

ocean. Different scenarios are explored to determine the parameters controlling the onset of convection in the magma ocean cumulate. We consider the case where fractional crystallization happens during the entire cooling history of the magma oceans as well as the case where no compositional fractionation occurs. We explore the classical case for which no matter crosses the boundary between the magma ocean and the solid cumulate, and also the case with a boundary that allows matter transfer accross it. The study is applied to the Earth, Mars, and the Moon.

2. Methods

We consider a mantle that is initially fully molten and crystallizes from the bottom or some intermediate depth upward. The goal of the present study is to determine the timescale for convection to start in the solid part of the mantle as the magma ocean crystallizes.

For the sake of simplicity, we assume the compaction length to be small and neglect the thickness of a mush layer at the phase change interface. Matter on one side of the boundary is entirely liquid while matter on the other side is entirely solid. We nonetheless allow for compositional fractionation to occur as the mantle crystallizes. The temperature at the solid/liquid boundary is denoted $\mathcal{T}_m$ and referred to as the melting temperature.

Depending on how the temperature profile in the magma ocean compares with the profile of the melting temperature, two situations can occur. Either the solidification of the ocean progresses from the bottom up, or the solidification starts from an intermediate depth leading to a setup in which the solid part of the mantle is surrounded by two magma oceans. In this second scenario, the crystallization of the surface magma ocean (SMO) is thought to be a lot faster than the crystallization of the basal magma ocean (BMO) (Labrosse et al., 2007).

We assume the solid mantle is a spherical shell of internal radius R^- and external radius R^+. Since the crystallization of the BMO is much slower than the crystallization of the SMO, we assume R^- to be constant even for the case where the solid shell is surrounded by two magma oceans. The presence or absence of a BMO however affects the boundary condition applied at the bottom boundary of the solid mantle (see section 2.4).

As the magma ocean cools down, R^+ increases to reach the total radius of the planetary body, denoted by R_T. The temperature at the top boundary of the solid follows the melting temperature. The composition of the solid changes as well with the radius if we assume fractional crystallization occurs. For the sake of simplicity, we only consider fractionation of iron. The mass fraction of FeO, denoted by C, varies between 0 (e.g. Forsterite) and 1 (e.g. Fayalite). Although simplistic, such a model allows us to study the effect of the density gradient due to fractional crystallization on the dynamics of the solid. Figure 1 shows the composition and temperature profiles at two different times. We assume the velocity of the freezing front $\dot{R}^+$ does not vary laterally and that the SMO is well mixed, the temperature and compositional fields in the resulting solid

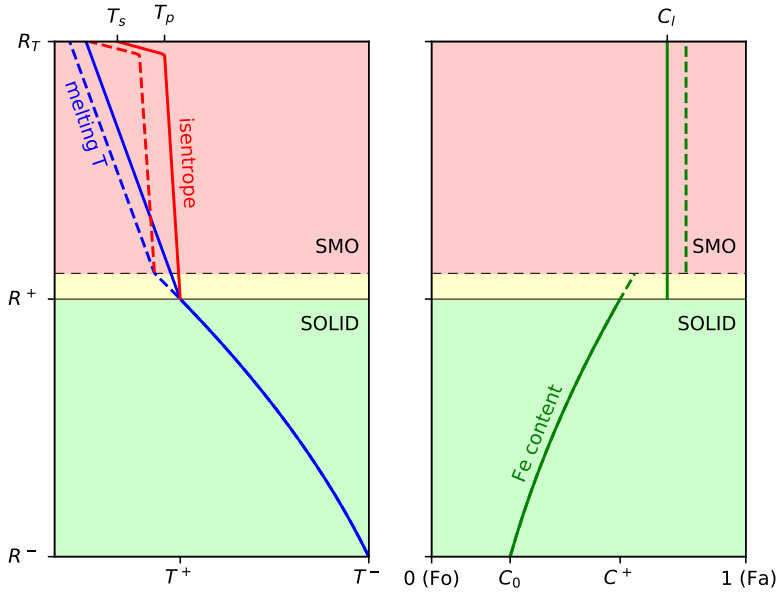

Figure 1: Temperature and composition reference profiles. Solid lines are the profiles at time t, dashed lines the profiles at time $t + \delta t$. The green area is the solid mantle at time t. The yellow area represents the part of the surface magma ocean (SMO, in red) that has crystallized during δt. All the annotations on the axes are written at time t (see table 1 for the meaning of symbols). Notice how the melting temperature decreases between the two instants owing to the enrichment in iron of the surface magma ocean. The slopes of the curves are exaggerated for readability purpose.

hence only vary with the radial position (as long as no solid-state convection operates).

In this section, we introduce the simple phase diagram we use to compute the resulting temperature and composition profiles in the solid under the assumption that no convection occurs in the solid (section 2.1). This serves as base state which stability against overturning motion is studied. We don't treat the full dynamics of the overturn but compute, using a linear stability analysis, the growth rate of an overturning instability to compare it to the crystallization rate of the magma ocean. The latter is computed using a magma ocean cooling model which gives R^+ as a function of time, as described in section 2.2.

2.1. Composition and temperature reference profiles

Under the assumption that no convection occurs during crystallization, one can determine the resulting temperature and compositional profiles in the cumulate. These profiles are used as reference profiles in order to perform the linear stability analysis (section 2.5).

Symbol	Description	Earth	Moon	Mars
Input parameters				
R^-	Internal radius of the solid shell	3871 km*	737 km	2090 km
R_T	Total radius of the planet	6371 km	1737 km	3390 km
$\mathcal{T}^-$	Temperature at the bottom boundary†	4500 K	1500 K	2400 K
$\mathcal{T}_\infty$	Black body equilibrium temperature	255 K	255 K	212 K
ε	Emissivity¶	10^{-4}	1	10^{-3}
g	Gravity acceleration	9.81 m/s^2	1.62 m/s^2	3.71 m/s^2
Ra_S	Rayleigh number of SMO	10^{30}	10^{28}	5×10^{28}
α	Thermal expansion coefficient	$10^{-5}\,\mathrm{K}^{-1}$		
C_p	Heat capacity	$10^3\,\mathrm{J\,K}^{-1}$		
κ	Thermal diffusivity	$10^{-6}\,\mathrm{m}^2/\mathrm{s}$		
L_h	Latent heat	$4 \times 10^5\,\mathrm{J\,kg}^{-1}$		
σ	Stefan-Boltzmann constant	$5.67 \times 10^{-8}\,\mathrm{Wm}^{-2}\mathrm{K}^{-4}$		
ρ	Reference density	$4 \times 10^3\,\mathrm{kg/m}^3$		
$\Delta\rho_m$	Solid/liquid density contrast	$2 \times 10^2\,\mathrm{kg/m}^3$		
η	Viscosity in the solid	$10^{18}\,\mathrm{Pa\,s}$		
C_{l_0}	Iron content of the primitive SMO†	0.1		
D	Solid/liquid partition coefficient of iron‡	0.6		
β	Compositional expansion coefficient	-0.33		
$\partial\mathcal{T}_m/\partial P$	Clapeyron slope	$2 \times 10^{-8}\,\mathrm{K\,Pa}^{-1}$		
$\partial\mathcal{T}_m/\partial C$	Dependence of $\mathcal{T}_m$ on iron content	$-700\,\mathrm{K}$		
Computed dimensional variables				
L_M	Final thickness of solid mantle $R_T - R^-$	2500 km	1000 km	1300 km
$\mathcal{T}_m$	Melting temperature	$\mathcal{T}_m(P, C)$ described by eq. (2.4)		
$\mathcal{T}^+$	Temperature at the top boundary	$\mathcal{T}^+(t)$ with eq. (2.5)		
$\mathcal{T}_p$	Potential temperature at the surface	$\mathcal{T}_p(t)$ with eq. (2.8)		
$\mathcal{T}_s$	Temperature at the surface of the planet	$\mathcal{T}_s(t)$ with eq. (2.9)		
R^+	External radius of the solid shell	$R^+(t)$ with eq. (2.10)		
L	Thickness of the solid shell	$L = R^+ - R^-$		
C_0	Iron content of the first solid	$KC_{l_0} = 0.06$		
C_l	Iron content of the SMO	$KC_l(t) = C^+(t)$ with eq. (2.2)		
τ_{Stokes}	Stokes time	$\eta L^2/(\Delta\rho g L_M^3)$		
Dimensionless numbers				
$\mathrm{Ra}(t)$	Thermal Rayleigh number	$\rho g\alpha\Delta T L^3/(\eta\kappa)$		
$\mathrm{Rc}(t)$	Compositional Rayleigh number	$\rho g\beta L^3/(\eta\kappa)$		
$W(t)$	Freezing front velocity (Peclet number)	$L\dot{R}^+/\kappa$		
$\Gamma(t)$	Thickness of the solid part	L/L_M		
$\Gamma_S(t)$	Thickness of the SMO	$(R_T - R^+)/L_M$		
$\Phi^\pm$	Phase change number§	10^{-2}; ∞		

Table 1: Symbols used in this paper. All quantities with a + superscript are evaluated at the top boundary (R^+), while quantities with a − superscript are evaluated at the bottom boundary (R^-). ¶ The emissivity values for the Earth and Mars are chosen so that the crystallization time scale of the SMO is of the order of 1 Myr (Lebrun et al., 2013). For the Moon, we neglect the effects of the atmosphere and assume a black body cooling. * This choice assumes a 400 km thick basal magma ocean. Using $R^- = 3471$ km does not change significantly the results. † From Andrault et al. (2011), ‡ from Andrault et al. (2012). § 10^{-2}: flow-through, ∞: non-penetrative. For the Moon and Mars, the possibility of a BMO is not considered and $\Phi^- = \infty$ (see section 2.4 for details).

We consider a magma ocean crystallizing from some depth R^- up to its top radius R_T. The mass fraction of the heavy component (FeO) is $C(r)$ in the solid and $C_l(t)$ in the liquid, assuming that no diffusion (nor convection) operates in the solid (therefore C does not depend on time) and convection mixes the liquid efficiently (therefore C_l depends only on time). At the freezing front, the phase relation is

$$C(R^+(t)) = DC_l(t) \tag{2.1}$$

with D the partition coefficient (considered constant) and $R^+(t)$ the time-evolving radius of the freezing interface.

Assuming the magma ocean undergoes fractional crystallization, the composition profile in the cumulate is exponential. At the radial position r it is

$$C(r) = \begin{cases} C_0 \left(\frac{{R_T}^3 - (R^-)^3}{{R_T}^3 - r^3} \right)^{1-D} & \text{if } r < R_s \\ 1 & \text{if } r > R_s, \end{cases} \tag{2.2}$$

with

$$R_s = \left((R^-)^3 C_0^{\frac{1}{1-D}} + {R_T}^3 \left(1 - C_0^{\frac{1}{1-D}} \right) \right)^{1/3} \tag{2.3}$$

the value of R^+ at which C_l reaches 1 (see appendix A for more details).

Since the diffusion timescale is much larger than the other time scales considered here, we assume the temperature profile in the cumulate stays close to the melting temperature. We take into account variations of the melting temperature $\mathcal{T}_m$ due to both the pressure and the composition. A higher concentration in iron leading to a lower melting temperature, the resulting temperature profile in the solid is steeper than a constant-concentration solidus when fractional crystallization is accounted for (Figure 1). The melting temperature $\mathcal{T}_m$ verifies:

$$\frac{\mathrm{d}\mathcal{T}_m}{\mathrm{d}r} = \frac{\partial \mathcal{T}_m}{\partial P}\frac{\partial P}{\partial r} + \frac{\partial \mathcal{T}_m}{\partial C}\frac{\partial C}{\partial r}. \tag{2.4}$$

With $\dfrac{\partial P}{\partial r} = -\rho g$ and eq. (2.2), one obtains

$$\frac{\mathrm{d}\mathcal{T}_m}{\mathrm{d}r} = -\rho g \frac{\partial \mathcal{T}_m}{\partial P} + 3C(1-D)\frac{r^2}{{R_T}^3 - r^3}\frac{\partial \mathcal{T}_m}{\partial C}. \tag{2.5}$$

For the sake of simplicity, we assume $\dfrac{\partial \mathcal{T}_m}{\partial P}$ and $\dfrac{\partial \mathcal{T}_m}{\partial C}$ to be constant (see table 1 for values).

We denote $T = \mathcal{T} - \mathcal{T}_{\text{isen}}$ the superisentropic temperature in the solid, with

$$\mathcal{T}_{\text{isen}} = \mathcal{T}^- \exp\left(\frac{\alpha g (R^- - r)}{C_p} \right) \tag{2.6}$$

the isentropic temperature profile in the solid, with α the coefficient of thermal expansion, g the acceleration of gravity and C_p the heat capacity. We

assume the variations of α, C_p and g with depth to be negligible. The reference superisentropic temperature (denoted $\bar{T}$) gradient is then:

$$\frac{\mathrm{d}\bar{T}}{\mathrm{d}r} = -\rho g \frac{\partial \mathcal{T}_m}{\partial P} + 3C(1-D)\frac{r^2}{{R_T}^3 - r^3}\frac{\partial \mathcal{T}_m}{\partial C} + \frac{\alpha g}{C_p}\mathcal{T}^- \exp\left(\frac{\alpha g(R^- - r)}{C_p}\right). \quad (2.7)$$

2.2. Crystallization time scale

Assuming the temperature profile in the SMO to be isentropic and neglecting variations of α, g and C_p with depth, the potential temperature at the surface is:

$$\mathcal{T}_p = \mathcal{T}^+ \exp\left(\frac{-\alpha g(R_T - R^+)}{C_p}\right). \quad (2.8)$$

Note that we are neglecting the temperature drop across the boundary layer at the bottom of the magma ocean. This is justified by the very small viscosity of the magma and the main buoyancy force coming from cooling to the atmosphere at the top surface.

King et al. (2012) showed that the scaling law for the heat flux in a rotating fluid (such as the surface magma ocean) depends on how the quantity $\mathrm{Ra}_S \mathrm{E}_S^{3/2} = \dfrac{\alpha g \Delta T \nu^{1/2}}{\kappa (2\Omega)^{3/2}}$ compares to 1, with E_S the Ekman number and Ra_S the Rayleigh number in the SMO. A conservative lower bound with the thermal expansivity $\alpha \sim 10^{-5}\,\mathrm{K}^{-1}$, the gravity $g \sim 10\,\mathrm{m/s^2}$, the super-isentropic temperature difference $\Delta T \sim 1\,\mathrm{K}$, the kinematic viscosity $\nu \sim 10^{-5}\,\mathrm{m^2/s}$, the thermal diffusivity $\kappa \sim 10^{-6}\,\mathrm{m^2/s}$ and the rotation rate $\Omega \sim 10^{-4}\,\mathrm{s}^{-1}$ is $\mathrm{Ra}_S \mathrm{E}_S^{3/2} \sim 10^5 \gg 1$. We then consider the heat flux is not controlled by rotation and scales as $\mathrm{Nu} = 0.16 \mathrm{Ra}_S^{2/7} \Gamma_S^{6/7}$ with $\Gamma_S = (R_T - R^+)/L$ the dimensionless thickness of the SMO (King et al., 2012). Note that this scaling does not depend on the Prandtl number in the range of values explored by King et al. (2012), i.e. $1 \leqslant \mathrm{Pr} \leqslant 100$. Since $\mathrm{Pr} \sim 10$ is a reasonable value for a magma ocean, we assume this scaling holds for our study. We neglect variations of Ra_S with time and assume the magma ocean behaves like a gray body at its upper surface. Heat flow conservation at the surface gives the following equation for the surface temperature $\mathcal{T}_s$:

$$\frac{k(\mathcal{T}_p - \mathcal{T}_s)}{L_M} 0.16 \mathrm{Ra}_S^{2/7} \Gamma_S^{-1/7} = \varepsilon \sigma (\mathcal{T}_s^4 - \mathcal{T}_\infty^4) \quad (2.9)$$

where $\mathcal{T}_\infty$ is the black body equilibrium temperature, σ is the Stefan-Boltzmann constant and ε the emissivity. The emissivity should depend on the atmosphere dynamics and composition (particularly its water content) and vary with time. Taking this effet into account would require an atmosphere model (e.g. Abe, 1997; Lebrun et al., 2013). For the sake of simplicity, we assume the emissivity to be constant, tuning its value to obtain a crystallization timescale that matches the ones of Lebrun et al. (2013) (see table 1 for values).

As the SMO crystallizes (i.e. R^+ increases with time), we assume the temperature at the top of the solid mantle $\mathcal{T}^+$ follows the solidus (eq. (2.5)), and

the temperature profile in the SMO follows an isentropic profile. As R^+ grows, two phenomena produce heat that should be evacuated: the crystallization itself with an associated latent heat L_h, and the cooling of the magma ocean. Assuming this heat is entirely evacuated through radiation in the atmosphere modeled as a gray body, one obtains the following equation:

$$\varepsilon\sigma R_T^2(\mathcal{T}_s^4-\mathcal{T}_\infty^4) = \rho L_h {R^+}^2 \frac{\mathrm{d}R^+}{\mathrm{d}t} - \rho C_p \frac{\mathrm{d}}{\mathrm{d}t}\left(\int_{R^+}^{R_T} \mathcal{T}^+ \exp\left(\frac{\alpha g(R^+-r)}{C_p}\right) r^2 \mathrm{d}r\right). \tag{2.10}$$

The last term of this equation can be developed (keeping in mind that the lower bound of the integral R^+ depends on time). This yields the time derivative of $\mathcal{T}^+$, which is written as a derivative with respect to R^+ using the chain rule. One obtains an ordinary differential equation on $R^+(t)$ whose numerical integration gives the position of the interface between the solid and the surface magma ocean as a function of time.

2.3. Set of dimensionless equations

$L = R^+ - R^-$, L_M^2/κ, κ/L, $\eta L^3/\kappa$, $\Delta T = T^- - T^+$ are used as scales for length, time, velocity, mass and temperature respectively. Note that R^+ and T^+ vary with time as the surface magma ocean crystallizes. $L_M = R_T - R^-$ is the thickness of the solid mantle once the SMO is entirely crystallized. Note that all scales depend on time except the one for time itself, which is why $\Gamma = L/L_M$ appears in the following equations. The dimensionless radial position is built as $1 + (r - R^-)/L$ so that it is between 1 and 2 at all times. Similarly, the dimensionless temperature is chosen as $(T - T^+)/\Delta T$ so that it is between 0 and 1 at all times.

Using the same symbols for dimensionless quantities, dimensionless conservation equations of mass, momentum, heat and iron fraction are written as:

$$\nabla \cdot \mathbf{u} = 0 \tag{2.11}$$

$$\mathbf{0} = -\boldsymbol{\nabla} p + \nabla^2 \mathbf{u} + \mathrm{Ra}\,(\Theta - \langle\Theta\rangle)\,\hat{\mathbf{r}} + \mathrm{Rc}\,(c - \langle c\rangle)\,\hat{\mathbf{r}} \tag{2.12}$$

$$\Gamma^2 \frac{\partial \Theta}{\partial t} + \mathbf{u}\cdot\boldsymbol{\nabla}(\Theta + \bar{T}) - \nabla^2\Theta = W\left((r-1)\frac{\partial\Theta}{\partial r} + \left(\frac{\partial \bar{T}}{\partial r}\right)^+ \Theta\right) \tag{2.13}$$

$$\Gamma^2 \frac{\partial c}{\partial t} + \mathbf{u}\cdot\boldsymbol{\nabla}(c + \bar{C}) = W(r-1)\frac{\partial c}{\partial r}. \tag{2.14}$$

$\mathbf{u}$ is the velocity field, p the dynamic pressure, Θ the temperature perturbation with respect to the reference profile $\bar{T}$ and c the composition perturbation with respect to the reference profile $\bar{C}$. $\langle x\rangle$ denotes the lateral average of the quantity x. Ra is the thermal Rayleigh number, Rc is the compositional Rayleigh number. The terms on the right hand side of eqs. (2.13) and (2.14) are due to the time dependence of the scales L and ΔT, which brings new advection terms associated with the change of frame, with $W = L\dot{R}^+/\kappa$ the dimensionless velocity of the freezing front. See table 1 for the definition and values of the various symbols.

Note that these equations are written under the assumption that $\dot{R}^- = 0$. Other terms would appear on the right hand side of eqs. (2.13) and (2.14) in the general case involving the crystallization of a basal magma ocean. For Earth's case, we assume the basal ocean crystallizes much slower than the surface ocean, and as such we neglect $\dot{R}^-$ (Labrosse et al., 2007). We assume the diffusion of the compositional field is negligible since the diffusion coefficient of composition is much smaller than that of heat. Moreover, diffusion of $\bar{T}$ is neglected while that of Θ is retained in order to ease the linear stability analysis. This is justified a posteriori by the fact that the diffusion timescale is much longer than the other timescales considered in this study.

2.4. Phase change boundary condition

In the classical Rayleigh-Bénard setup, convecting matter arriving near an horizontal boundary forms a topography whose height is limited by the weight viscous forces can sustain. This topography is often neglected and a non-penetrative boundary condition is assumed at the interface ($u_r(R^+) = 0$). However, in the system studied here, the boundary between the magma ocean and the cumulate is a phase change interface. A topography of the solid with respect to the equilibrium position of the solid/liquid interface can then be eroded by melting or freezing. Provided that the melting/freezing time is short compared to the time needed to build the topography by viscous forces, it is thus possible to have a non-zero normal velocity accross the interface. This is taken into account with the help of the boundary condition introduced for the inner core by Deguen et al. (2013). This boundary condition, which translates the continuity of normal stress across the interface, is written in dimensional form as:

$$\Delta\rho_m g \tau_\phi u_r + 2\eta \frac{\partial u_r}{\partial r} - p = 0. \tag{2.15}$$

where $\Delta\rho_m$ is the density difference between the solid and liquid phases and τ_ϕ is the phase change timescale. Note that our definition of the dynamic pressure (defined here as $p = P - \langle P \rangle$) differs from that of $\hat{p}$ used by Deguen et al. (2013). The laterally constant term $\Delta\rho_m g \tau_\phi \dot{R}$ is thus included in p instead of explicitly appearing in the boundary condition. The dimensionless form of the boundary condition is

$$\pm\Phi^{\pm} u_r + 2\frac{\partial u_r}{\partial r} - p = 0 \tag{2.16}$$

where Φ is the phase change number defined as:

$$\Phi^{\pm} = \frac{|\Delta\rho_m|^{\pm} g L \tau_\phi}{\eta} \tag{2.17}$$

(the superscript $^+$ denotes the interface between the SMO and the solid at R^+ while the superscript $^-$ denotes the interface between the BMO and the solid at R^-). Moreover, the continuity of tangential stress is simply written as a classic free-slip boundary condition.

The phase change timescale τ_ϕ is related to the time needed to transport latent heat in the magma ocean from the areas that freeze to the areas that melt (Deguen et al., 2013):

$$\tau_\phi = \frac{\rho L_h}{(\rho - \Delta\rho_m)^2 C_p (\partial_P \mathcal{T}_m - \partial_P \mathcal{T}_{\text{isen}}) g u'} \tag{2.18}$$

where u' is the velocity scale in the magma ocean. A reasonable value for the latter is $u' \sim 1\,\text{m}\,\text{s}^{-1}$ (Lebrun et al., 2013). Using nominal values for the other parameters, we find that $\tau_\phi \sim 10^4\,\text{s}$. Plugging this in the expression of the phase change parameter eq. (2.17) yields $\Phi \sim 10^{-5}$.

The phase change number Φ compares the phase change timescale τ_ϕ (i.e. the time needed to erode topography via melting and freezing) to the viscous timescale (i.e. the time needed to build topography with viscous forces). The value of Φ allows to tune continuously the boundary condition between a non-penetrative classical condition ($\Phi \to \infty$) and a fully permeable condition ($\Phi \to 0$). Although this number should depend on time since L depends on time and τ_ϕ depends also on time but in a non trivial way, it is kept constant in this study. Two extreme values are tested for the SMO/solid interface: $\Phi = \infty$ which leads to the classical non-penetrative boundary condition and $\Phi = 10^{-2}$ which leads to a flow-through boundary (we use this value rather than 10^{-5} because the resolution of radial modes is more computationally demanding as Φ decreases, while the overturn timescale is not affected as shown in the results). For the Earth, these two values are also considered at the bottom of the solid, accounting for the possible presence of a basal magma ocean (BMO, Labrosse et al., 2007). For Mars and the Moon, we do not consider the possibility of a BMO and the bottom interface is hence non-penetrative, $u_r(R^-) = 0$. Rather than being realistic, these extreme constant values are used to study how the possibility of melting and freezing at the interface affects the stability of the solid, both in terms of onset time of overturn and preferred mode of motion. The estimated nominal value being $\Phi \sim 10^{-5}$, we expect the real system should be closer to the flow-through case than to the classical non-penetrative case.

2.5. Determination of overturn timescale

We start from a completely molten primitive mantle ($R^+ = R^-$ and $\mathcal{T}^+ = \mathcal{T}^-$). We numerically integrate eq. (2.10) to obtain R^+ as a function of time (the potential surface temperature $\mathcal{T}_p$ and the surface temperature $\mathcal{T}_s$ are computed using eq. (2.8) and eq. (2.9)).

At each timestep of this integration, we compute the reference temperature and composition profiles in the solid as shown in section 2.1 as well as the dimensionless numbers $\text{Ra}(t)$, $\text{Rc}(t)$, $W(t)$ and $\Gamma(t)$. Using a Chebyshev-collocation approach (e.g. Guo et al., 2012; Canuto et al., 1985), the set of linearized equations around the reference state is written as an eigenvalue problem (see appendix B). Solving numerically this problem yields the growth rate and shape of the most unstable mode of overturn. The inverse of that growth rate is the timescale for convection to set in in the solid shell. We compute this

timescale at each timestep of the evolution of the SMO. By comparing this timescale with the corresponding time in the evolution of the SMO, we can assess whether convection is able to take place before the entire magma ocean is crystallized. Three different models are considered for the bulk of the solid:

1. full model: compositional, thermal, and moving frame terms are taken into account;
2. thermal model: compositional terms are left out, modeling the ideal case where no fractional crystallization occurs and the sources of instability are purely thermal (eq. (2.14) and the corresponding buoyancy term in eq. (2.12) are ignored);
3. frozen-time model: moving frame terms (right-hand-side of eqs. (2.13) and (2.14)) are left out, resulting in a frozen-time approach where all long term evolution terms are ignored when studying the stability of the system at a given instant.

We also compare the timescale obtained by linear stability analysis with the Stokes time $\tau_{\text{Stokes}} = \eta L^2/(\Delta\rho g L_M^3)$ computed at each time to check whether this time is a relevant proxy of the stability of the solid mantle.

3. Results

The destabilization timescales for the Earth, Mars, and the Moon with various boundary conditions along with the time needed to crystallize the remaining SMO are shown on Figure 2. Comparison of the destabilization timescales obtained for various bulk setups and boundary conditions yields information regarding their contribution to the destabilization of the solid.

The simplest cases are the one neglecting the compositional effects on density. For such cases, the destabilization timescale tends to infinity for a given non-zero thickness of crystallized mantle. This thickness corresponds to the one needed for instabilities to overcome diffusion of perturbations of the reference state. In other words, it corresponds to the thickness above which the Rayleigh number in the solid part is above the critical Rayleigh number. For the Moon, this thickness is never reached and the Moon's mantle stays stable with respect to purely thermal convection. For the Earth and Mars, this thickness is reached rather early, after $\sim 500\,\text{km}$ of solid mantle is formed. As crystallization progresses, the thickness and the temperature contrast between the top and the bottom of the solid mantle increase. The available buoyancy in the system therefore increases. This leads to a strong decrease of the destabilization timescale, which becomes much shorter than the time needed to crystallize the remaining surface magma ocean (up to 6 orders of magnitude, depending on which boundary conditions are considered). This suggests that even in the purely thermal case, solid-state convection sets in before the mantle is completely crystallized for planets larger than Mars.

The cases taking compositional effects on density into account are always unstable. This contrasts with the purely thermal cases and is due to the fact

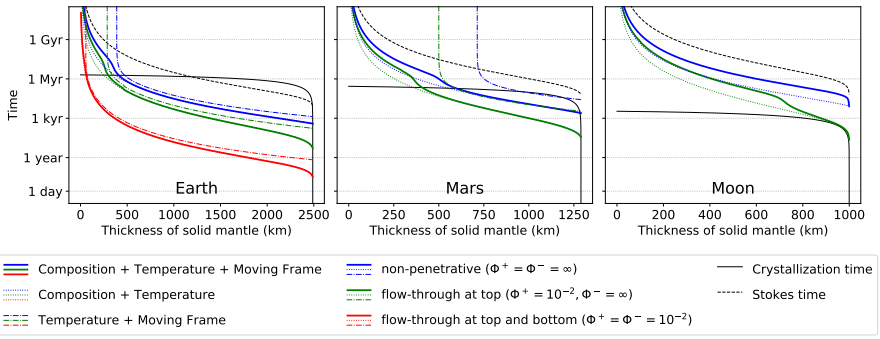

Figure 2: Growth time of the most unstable mode as a function of the crystallized mantle thickness for the Earth, Mars, and the Moon. The solid black line is the time necessary to crystallize the remaining surface magma ocean. Colors represent different boundary conditions: both horizontal boundaries non-penetrative (blue); flow-through boundary condition between the solid and the surface magma ocean to model the possibility of melting and freezing (see section 2.4 for details) (green); and flow-through boundary conditions for both horizontal boundaries assuming the presence of a basal magma ocean (red). Linestyles represent different approximations regarding compositional effects (fractional crystallization and effect on density) and moving frame contributions: both are taken into account (solid lines), compositional effects are neglected (dash-dotted lines), or moving frame terms are neglected (dotted lines). The black dashed line is the Stokes time for each thickness, given for comparison.

that diffusion of the composition field is neglected. There is no mechanism to damp perturbations around the reference state, the latter is hence always unstable. Similarly to what is observed for the thermal cases, the destabilization timescale drops dramatically as the solid mantle thickens. For the Earth and Mars, the destabilization timescale ends up being shorter than the crystallization time of the remaining SMO by several orders of magnitude. The case where moving frame terms are neglected exhibits a shorter destabilization time scale at small thickness. The moving frame terms play a stabilising role only at the begining of mantle crystallization for the Earth and Mars but are significant through the entire Moon's mantle crystallization. The stabilising effect of the moving terms can be understood from the energy conservation eq. (2.13). Taking a temperature perturbation $\theta > 0$ and the associated velocity perturbation $u_r > 0$, one can notice there is a competition between the advection term $u_r \partial_r \bar{T} < 0$ and the moving frame term $W(r-1)\partial_r \theta$ whose average is negative. The same reasoning can be made with a negative perturbation and on the iron conservation eq. (2.14).

For the Moon, the destabilization timescale is always greater than the time needed to crystallize the SMO. However, it should be noted that in this study the time to crystallize the SMO is computed assuming a well-mixed SMO with a surface behaving like a black body. The formation of a light solid crust enriched in plagioclase when around 80% of the SMO is crystallized is expected to slow down the solidification of the SMO by a few million years (e.g. Elkins-Tanton et al., 2011). This would leave enough time for convection to set in in the solid

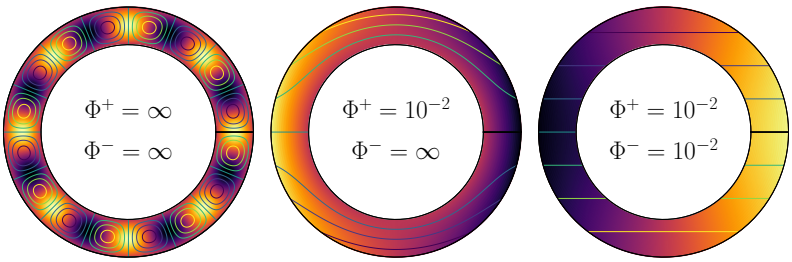

(a) classical case (b) flow-through at top (c) flow-through at top and bottom

Figure 3: Most unstable convection modes for the Earth when a 1700 km thick mantle has crystallized, for different boundary conditions represented by the values of the Φ parameters at the top and the bottom, as indicated. The dark zones represent negative temperature anomalies while the bright zones represent positive temperature anomalies. The streamlines are superimposed. Note that the linear stability analysis offers no constraint on the orientation and amplitude of these modes, only their harmonic degree and radial shape. (a): both boundaries non-penetrative, the convection rolls have an aspect ratio approximatively equal to 1; (b): flow-through top boundary, the flow pattern is of spherical harmonic degree one, the streamlines go through the top boundary but go around the central part; (c): flow-through conditions at both boundaries, the flow pattern is of spherical harmonic degree one, the streamlines go through both boundaries, resulting in a translation mode of convection. Similar behavior is obtained for the other bodies.

since the destabilization timescale we find is much shorter than that.

The three boundary conditions exhibits different destabilization timescales. The case where both boundaries are non-penetrative (which is the case classically considered) needs more time to destabilize than the case where the boundary between the surface magma ocean and the solid allows melting and freezing. Convective patterns obtained with a flow-through boundary are substantially different than the classical ones (Figure 3). Aspect-ratio-1 rolls are obtained with classical boundary conditions. However, when the top boundary allows phase change, a spherical-harmonic-degree-1 near-translation mode develops. Matter freezes on one side of the spherical shell, goes around the core or basal magma ocean, and melts on the other side. In the case with a basal magma ocean and its boundary with the solid of flow-through type, matter also crosses the inner boundary of the spherical shell, resulting in a true translation mode. These two translation modes involve very little or no deformation of the solid compared to the classical case, and therefore less viscous forces acting against convection. This explains the smaller destabilization timescale associated with these modes as well as the lower critical thickness in the purely thermal case.

Figure 4 shows the transition between the non-penetrative and the flow-through regime occurs over a rather short range of values of the phase change number. $\Phi^+ \lesssim 1$ leads to near-translation while $\Phi^+ \gtrsim 100$ leads to classical aspect-ratio-one rolls.

A notable feature on Figure 2 is the steep decrease of the destabilization

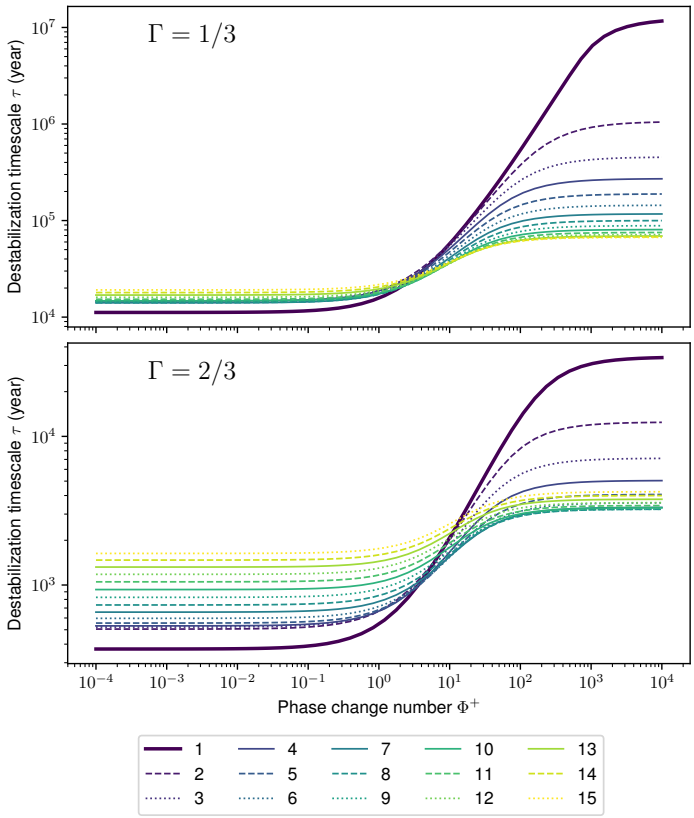

Figure 4: Destabilization timescale of several harmonics degree ($l = 1$ to 15) as a function of the phase change number value for the Earth. The bottom boundary is non-penetrative. Top: 833 km are crystallized (mid-radius $\bar{r} \sim 4288$ km), bottom: 1667 km are crystallized (mid-radius $\bar{r} \sim 4704$ km). The most unstable mode is the one with the shortest destabilization timescale. One can notice that in the non-penetrative case ($\Phi^+ \to \infty$), the most unstable mode corresponds to aspect-ratio-1 rolls. The typical roll size of the most unstable mode ($\bar{r}\pi/l$) is roughly 900 km for the top case ($l = 15$) and 1850 km for the bottom case ($l = 8$). However, with a flow-through boundary ($\Phi^+ \to 0$), the most unstable mode is the near-translation mode for both cases.

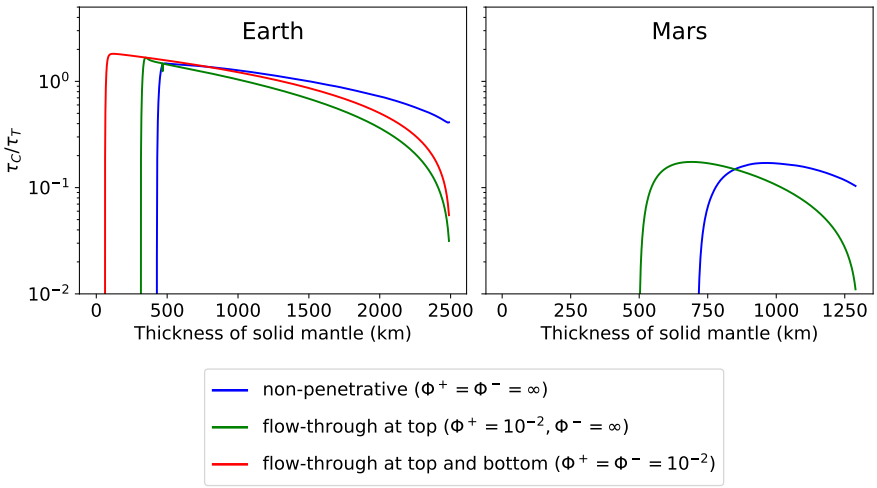

Figure 5: Ratio between the destabilization timescale obtained for the purely compositional case τ_C (thermal terms are left out) and the timescale obtained for the purely thermal case τ_T (compositional terms are left out). When this ratio is above one, it means the thermal reference profile is more unstable than the compositional reference profile. The Moon is not shown here since the purely thermal case is never unstable ($\tau_T \to \infty$). The colors are the same as in Figure 2, blue: non-penetrative condition for both horizontal boundaries ($\Phi^{\pm} = \infty$); green: flow-through condition at the boundary between the solid and the surface magma ocean; and red: flow-through condition at both horizontal boundaries.

timescales at the end of the crystallization when compositional terms are taken into account. That decrease is due to the strong (i.e. very unstable) compositional gradient appearing at the end of the crystallization. It does not affect the destabilization timescale obtained with non-penetrative boundary conditions; this can be explained by the fact that the strong compositional gradient is in a very thin layer at the top of the domain where vertical velocities vanish, and therefore does not contribute to the driving of the down- and up-welling currents.

A comparison between the purely thermal and purely compositional cases for the Earth and Mars is shown on Figure 5. The ratio between the destabilization timescales for theses two cases is 0 before the critical thickness for the purely thermal case is reached. For Mars, the compositional profile is always more unstable than the thermal profile and controls the destabilization timescale of the system. For the Earth, however, the ratio between the two cases is fairly close to 1 for a large part of the crystallization history: neither the thermal nor the compositional profile dominates the destabilization timescale of the system.

Figure 6 shows that the destabilization timescale τ_{LSA} is proportional to the Stokes time $\tau_{\mathrm{Stokes}} = \eta L^2/(\Delta\rho g L_M^3)$. Two effects alter this relation: moving frame terms whose effects are not included in the Stokes time, and the strong compositional gradient at the end of the crystallization whose effects depend

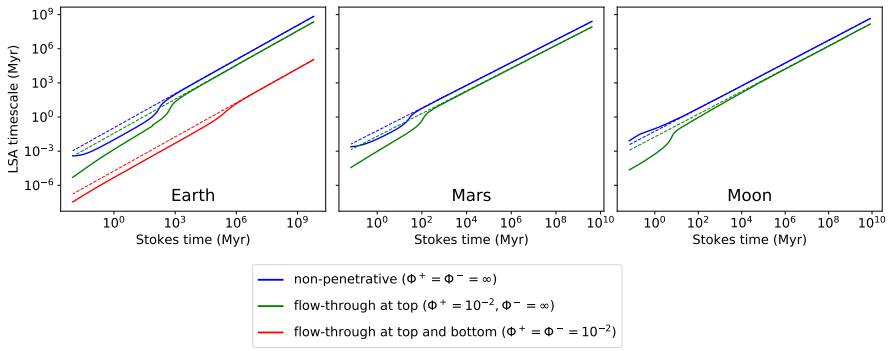

Figure 6: Growth time of the most unstable mode versus the Stokes time for the Earth, Mars, and the Moon. The solid line is the destabilization timescale obtained with the linear stability analysis τ_{LSA} (case with all terms accounted for). The dashed lines correspond to $\tau_{\mathrm{LSA}} \propto \tau_{\mathrm{Stokes}}$. Composition, temperature and moving frame terms are all taken into account. The colors are the same as in Figure 2, blue: non-penetrative condition for both horizontal boundaries ($\Phi^{\pm} = \infty$); green: flow-through condition at the boundary between the solid and the surface magma ocean; and red: flow-through condition at both horizontal boundaries.

on the boundary condition. It should be noted that the ratio $\tau_{\mathrm{LSA}}/\tau_{\mathrm{Stokes}}$ depends on the body and the boundary conditions considered. Notably, permeable boundary conditions lead to a decrease of τ_{LSA}.

4. Discussion

We showed for the Earth and Mars that the growth timescale of convective instabilities in a crystallizing mantle from the bottom up is several orders of magnitude smaller than the time needed to fully crystallize that mantle. This holds even without taking into account fractional crystallization and the unstable density gradient it induces. This contrasts with the assumptions made in several studies (Hess and Parmentier, 1995; Elkins-Tanton et al., 2003; Tosi et al., 2013) where the overturn is assumed to take place because of the compositionally induced density gradient after the entire mantle is crystallized. The numerical simulations performed by Ballmer et al. (2017) for Earth-like objects lead to a destabilization of the solid after a few Myr, and those performed by Maurice et al. (2017) for Mars-like objects lead to a destabilization after roughly 1 Myr. These times are not easily comparable to the timescales we compute via linear stability analysis since the physical problems are different in non-trivial ways: the simulations of Ballmer et al. (2017) are in a 2D aspect-ratio-1 cartesian box, those of Maurice et al. (2017) are in cylindrical geometry with a variable viscosity, a melt extraction mechanism and a solidus temperature that depends only on pressure. However, despite these differences, the destabilization time uncovered by these simulations are rather similar to the one we predict for the non-penetrative cases: of the order of 1 Myr for the Earth and 0.5 Myr for

Mars. This confirms the linear growth rate of instabilities is a relevant proxy for the timescale at which convection sets in.

Moreover, allowing transfer of matter via melting and freezing at the interface between the solid and the surface magma ocean reduces dramatically the timescale with which solid-state convection can set in. It also changes the shape and harmonic degree of the most unstable mode: a degree-one translation mode is preferred. Therefore, the possibility of melting and freezing at the interface should be accounted for when studying the overturn of the primitive mantle of planetary bodies. For example, the case of the Moon is an interesting potential application. This body has a strong dichotomy: the near-side presents more mare basalts, more KREEP material, and a thinner crust than the far-side. Wasson and Warren (1980) already proposed that such features could be due to a slower cooling of the lunar magma ocean on the near side than on the far-side. A permeable boundary would allow the solid mantle to overturn with a dominant degree-one before the entire crystallization of the mantle (keeping in mind that the end of the crystallization is much slower than what we predict with our simple model, see Elkins-Tanton et al. (2011)). The mechanisms proposed to build a degree 1 at the scale of the Moon involve the dynamics of an entirely crystallized lunar mantle (e.g. Parmentier et al., 2002; Zhong et al., 2000). The possibility to form a degree one while the crystallization of the magma ocean is still ongoing is therefore worth exploring with more complete models to test whether this dominant degree-one can be conserved after crystallization of the magma ocean and/or helps the development of degree-one instabilities such as the ones predicted in the aforementioned studies. It is also tempting to associate the degree-one feature of Mars (the Marsian dichotomy) to the same process but, as explained above, the first degree-one overturn of the solid mantle is expected to happen long before its complete crystallization. Secondary overturning instabilities are possible after the first one that we cannot investigate with the tools presented above. A more complete study investigating the finite amplitude dynamics is necessary to understand the implications of this work to planets larger than the Moon.

It should be noted that several parameters involved in the problem are badly constrained. The viscosity of the solid mantle and even its rheology is such a parameter. It is highly dependent on how close the temperature in the solid is from the solidus and could easily vary by a few orders of magnitude (e.g. Solomatov, 2015). Since the destabilization timescale scales as the Stokes time (Figure 6), it is directly proportional to the viscosity and could therefore vary by a few orders of magnitude. The strong relation between the viscosity of the cumulate and the overturn scaling has been investigated by Ballmer et al. (2017): their numerical experiments confirm the overturn onset scales as the Stokes time. It should be noted that our flow-through boundary conditions does not affect this result, it only reduces the proportionality factor between the Stokes time and the growth time of instabilities (Figure 6). This validates the general approach proposed by Boukaré et al. (2018) to assess whether solid-state convection sets in before the magma ocean is entirely crystallized: they compare the Stokes time with the time needed to crystallize the magma ocean and their numeri-

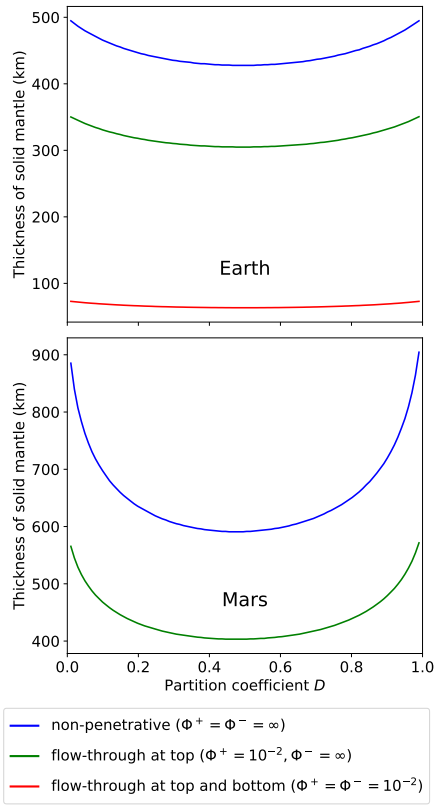

Figure 7: Thickness of the solid cumulate at which the destabilization timescale equals the time needed to crystallize the rest of the SMO for several values of the partition coefficient, $D \in [0.01, 0.99]$. The Moon is not shown here since the destabilization timescale is greater than the time needed to crystallize the SMO. The colors are the same as in Figure 2, blue: non-penetrative condition for both horizontal boundaries ($\Phi^{\pm} = \infty$); green: flow-through condition at the boundary between the solid and the surface magma ocean; and red: flow-through condition at both horizontal boundaries.

cal experiments yields that syn-crystallization convection is possible when the ratio between these two times exceeds $\sim 5 \times 10^4$. This value however was determined with non-penetrative boundary conditions, the actual threshold should be a few orders of magnitude higher (meaning syn-crystallization convection is allowed for shorter solidification timescales) since the flow-through boundary condition leads to a faster destabilization of the cumulate for the same Stokes time. Another aspect that deserves care is that for Earth-sized bodies, the Stokes time should incorporate both the thermal and compositional density constrasts. Boukaré et al. (2018) compare the "compositional" Stokes time with the solidification timescale; while this is perfectly valid for the Moon and Mars for which the thermal density contrast is much smaller than the compositional one, this does not hold for the Earth where both terms have similar magnitudes (Figure 5). The tremendous importance of the viscosity is why a viscosity of 10^{18} Pa s is assumed in this study since it is a higher bound for the near-solidus viscosity (see Solomatov, 2015, and references therein) and gives the most conservative estimate for the destabilizing time. The viscosity could be significantly lower if the melt fraction is important in the cumulate, Solomatov (2015) suggests 10^{14} Pa s as a lower bound at 40% melt fraction (roughly the rheological transition). Another potential effect of viscosity that is neglected in the study is dynamical: since solid state convection occurs during the crystallization of the magma ocean, the temperature in the solid departs from the solidus temperature profile and as a result the viscosity increases. Moreover, the compositional profile becomes gravitationally stable with iron-enriched heavy material being transported from the top to the bottom of the solid. These two effects combined may lead to the stopping of the solid state convection (Solomatov, 2015). Depending on the size of the magma ocean considered, it could then be possible either that the magma ocean crystallizes completely before convection may start again in the solid, or that convection sets in again in the solid before it is entirely crystallized. Studying this scenario requires a more complex method that a simple linear stability analysis since it involves a non-linear feedback between the dynamics of the solid part and its viscosity, temperature, and compositional fields.

Another unconstrained parameter is the partition coefficient of iron between the solid and liquid. An exploration of this parameter shows that the effect of the partition coefficient is rather limited for the Earth, and slightly more important for Mars (Figure 7). This is in agreement with Figures 2 and 5 showing the difference between the purely thermal case (corresponding to the extreme value $D = 1$) and the purely compositional case is rather small for the Earth but more important for Mars.

Finally, our choice of a constant emissivity results in a roughly constant solidification rate, whereas more sophisticated cooling models including an atmosphere predict most of the mantle crystallizes quickly, and the solidification slows down when only a shallow magma ocean remains. Although such effects are important to build realistic solidification models, they should not affect dramatically our results. Indeed, a faster crystallization at the beginning would lead to a destabilization of the solid mantle at a larger thickness, but we expect this

difference to be small since the destabilization timescale is rapidly much lower than the solidification timescale.

5. Conclusions

Upward crystallization of the silicate mantle of planets within a magma ocean is expected to produce a unstably stratified situation, because of both temperature and composition. In this study, we have addressed the question of whether the overturning instability develops faster than the time it takes to crystallize the magma ocean. To that end, we have developed a linear stability analysis tool to compute the growth rate of the fastest overturning mode and studied systematically the effect of the most important parameters: the planet's size (Moon to Earth size), the partition coefficient and the type of boundary condition between the solid and the liquid. In particular, we have introduced a boundary condition that accounts for the possibility of melting and freezing at the interface between the solid mantle and the magma ocean.

This study shows convection is likely to start in the solid mantle of the Earth, Mars and the Moon before the entire crystallization of the surface magma ocean. Evolution models of the primitive mantle of planetary bodies should therefore account for convection and the associated mixing in the solid part of the crystallizing mantle.

This result holds for the Earth and Mars even without fractional crystallization and the unstable compositional gradient it creates in the cumulate. The value of the partition coefficient is found to have little impact on the timing of mantle overturn.

The timescale at which convection sets in scales as the Stokes time. Specifically, it is proportional to the viscosity of the solid. However, it should be kept in mind that these results are obtained assuming a newtonian rheology and a constant viscosity in the solid mantle. Given the central role of viscosity in this problem, better knowledge of the viscosity and rheology of the primitive solid mantle is of primary importance to study its dynamics.

Finally, the possibility of exchange of matter between the solid mantle and the magma ocean(s) should be accounted for in dynamical models of the primitive mantle since it greatly alters the pattern of convection as well as the destabilization timescale. It could even be a way of producing degree-one structures such as the ones observed on the Moon and Mars.

Acknowledgements

We thank the editor Bruce Buffet and an anonymous reviewer for their useful remarks that helped to improve the clarity of our paper. This study is funded by the French Agence Nationale de la Recherche (grant number ANR-15-CE31-0018-01, MaCoMaOc).

References

Abe, Y., 1997. Thermal and chemical evolution of the terrestrial magma ocean. Phys. Earth Planet. Inter. 100, 27–39. doi:10.1016/S0031-9201(96)03229-3.

Andrault, D., Bolfan-Casanova, N., Nigro, G.L., Bouhifd, M.A., Garbarino, G., Mezouar, M., 2011. Solidus and liquidus profiles of chondritic mantle: Implication for melting of the Earth across its history. Earth and Planetary Science Letters 304, 251–259. doi:10.1016/j.epsl.2011.02.006.

Andrault, D., Petitgirard, S., Lo Nigro, G., Devidal, J.L., Veronesi, G., Garbarino, G., Mezouar, M., 2012. Solid–liquid iron partitioning in Earth's deep mantle. Nature 487, 354–357. doi:10.1038/nature11294.

Ballmer, M.D., Lourenço, D.L., Hirose, K., Caracas, R., Nomura, R., 2017. Reconciling magma-ocean crystallization models with the present-day structure of the Earth's mantle. Geochemistry, Geophysics, Geosystems 18, 2785–2806. doi:10.1002/2017GC006917.

Boukaré, C., Parmentier, E., Parman, S., 2018. Timing of mantle overturn during magma ocean solidification. Earth and Planetary Science Letters 491, 216–225. doi:10.1016/j.epsl.2018.03.037.

Boukaré, C.E., Ricard, Y., Fiquet, G., 2015. Thermodynamics of the MgO-FeO-SiO2 system up to 140 GPa: Application to the crystallization of Earth's magma ocean. Journal of Geophysical Research: Solid Earth 120, 6085–6101. doi:10.1002/2015JB011929.

Canuto, C., Yousuff Hussaini, M., Quarteroni, A., Zang, T.A., 1985. Spectral Methods in Fluid Dynamics. Springer Series in Computational Physics.

Deguen, R., 2013. Thermal convection in a spherical shell with melting/freezing at either or both of its boundaries. Journal of Earth Science 24, 669–682. doi:10.1007/s12583-013-0364-8, arXiv:arXiv:1303.4513v1.

Deguen, R., Alboussière, T., Cardin, P., 2013. Thermal convection in Earth's inner core with phase change at its boundary. Geophysical Journal International doi:10.1093/gji/ggt202.

Elkins-Tanton, L.T., Burgess, S., Yin, Q.Z., 2011. The lunar magma ocean: Reconciling the solidification process with lunar petrology and geochronology. Earth and Planetary Science Letters 304, 326–336. doi:10.1016/j.epsl.2011.02.004.

Elkins-Tanton, L.T., Parmentier, E.M., Hess, P.C., 2003. Magma ocean fractional crystallization and cumulate overturn in terrestrial planets: Implications for Mars. Meteoritics & Planetary Science 38, 1753–1771. doi:10.1111/j.1945-5100.2003.tb00013.x.

Elkins-Tanton, L.T., Zaranek, S.E., Parmentier, E.M., Hess, P.C., 2005. Early magnetic field and magmatic activity on Mars from magma ocean cumulate overturn. Earth and Planetary Science Letters 236, 1–12. doi:10.1016/j.epsl.2005.04.044.

Fiquet, G., Auzende, A.L., Siebert, J., Corgne, A., Bureau, H., Ozawa, H., Garbarino, G., 2010. Melting of peridotite to 140 gigapascals. Science (New York, N.Y.) 329, 1516–8. doi:10.1126/science.1192448.

Guo, W., Labrosse, G., Narayanan, R., 2012. The Application of the Chebyshev-Spectral Method in Transport Phenomena. Springer-Verlag Berlin. doi:10.1007/978-90-481-9809-2.

Hess, P.C., Parmentier, E.M., 1995. A model for the thermal and chemical evolution of the Moon's interior: implications for the onset of mare volcanism. Earth and Planetary Science Letters 134, 501–514. doi:10.1016/0012-821X(95)00138-3.

King, E.M., Stellmach, S., Aurnou, J.M., 2012. Heat transfer by rapidly rotating Rayleigh–Bénard convection. Journal of Fluid Mechanics 691, 568–582. doi:10.1017/jfm.2011.493.

Labrosse, S., Hernlund, J.W., Coltice, N., 2007. A crystallizing dense magma ocean at the base of the Earth's mantle. Nature 450, 866–869. doi:10.1038/nature06355.

Labrosse, S., Morison, A., Deguen, R., Alboussière, T., 2018. Rayleigh – Bénard convection in a creeping solid with melting and freezing at either or both its horizontal boundaries. Journal of Fluid Mechanics 846, 5–36. doi:10.1017/jfm.2018.258.

Lebrun, T., Massol, H., Chassefière, E., Davaille, A., Marcq, E., Sarda, P., Leblanc, F., Brandeis, G., 2013. Thermal evolution of an early magma ocean in interaction with the atmosphere. Journal of Geophysical Research E: Planets 118, 1155–1176. doi:10.1002/jgre.20068.

Maurice, M., Tosi, N., Samuel, H., Plesa, A.C., Hüttig, C., Breuer, D., 2017. Onset of solid-state mantle convection and mixing during magma ocean solidification. Journal of Geophysical Research: Planets doi:10.1002/2016JE005250.

Parmentier, E., Zhong, S., Zuber, M., 2002. Gravitational differentiation due to initial chemical stratification: origin of lunar asymmetry by the creep of dense KREEP? Earth and Planetary Science Letters 201, 473–480. doi:10.1016/S0012-821X(02)00726-4.

Ribe, N., 2007. Analytical approaches to mantle dynamics. Treatise on Geophysics .

Ricard, Y., Vigny, C., 1989. Mantle dynamics with induced plate tectonics. Journal of Geophysical Research 94, 17543–17559. doi:10.1029/JB094iB12p17543.

Solomatov, V., 2015. Chapter 4 Magma Oceans and Primordial Mantle Differentiation, in: Treatise on Geophysics. Elsevier. volume 9, pp. 91–119.

Thomas, C.W., Asimow, P.D., 2013. Direct shock compression experiments on premolten forsterite and progress toward a consistent high-pressure equation of state for CaO-MgO-Al2O3-SiO2-FeO liquids. J. Geophys. Res. 118, 5738–5752. doi:10.1002/jgrb.50374.

Tosi, N., Plesa, A.C., Breuer, D., 2013. Overturn and evolution of a crystallized magma ocean: A numerical parameter study for Mars. Journal of Geophysical Research E: Planets 118, 1512–1528. doi:10.1002/jgre.20109.

Wasson, J.T., Warren, P.H., 1980. Contribution of the Mantle to the Lunar Asymmetry , 752–771doi:10.1016/0019-1035(80)90142-6.

Zhang, N., Parmentier, E.M., Liang, Y., 2013. A 3-D numerical study of the thermal evolution of the Moon after cumulate mantle overturn: The importance of rheology and core solidification. Journal of Geophysical Research: Planets 118, 1789–1804. doi:10.1002/jgre.20121.

Zhong, S., Parmentier, E.M., Zuber, M.T., 2000. A dynamic origin for the global asymmetry of lunar mare basalts. Earth and Planetary Science Letters 177, 131–140. doi:10.1016/S0012-821X(00)00041-8.

A. Composition profile resulting from the fractional crystallization of the surface magma ocean

Conservation of the heavy component implies that

$$\frac{\mathrm{d}}{\mathrm{d}t}\left(\int_{R^-}^{R^+} C(r) r^2 \mathrm{d}r + \frac{1}{3}\left({R_T}^3 - {R^+}^3\right) C_l\right) = 0, \tag{A.1}$$

where no compressibility effect on density is considered, allowing the bulk density to drop out of the equation. Using eq. (2.1) and $\dot{C}_l = \dot{R^+}\dfrac{\mathrm{d}C_l}{\mathrm{d}R^+}$, assuming $\dot{R^+} > 0$ at all time and R^- constant:

$$\frac{1}{C_l}\frac{\mathrm{d}C_l}{\mathrm{d}R^+} = 3(1-D)\frac{{R^+}^2}{{R_T}^3 - {R^+}^3}. \tag{A.2}$$

Using eq. (2.1), eq. (A.2) can be written for C:

$$\frac{1}{C}\frac{\mathrm{d}C}{\mathrm{d}R^+} - \frac{1}{D}\frac{\mathrm{d}D}{\mathrm{d}R^+} = 3(1-D)\frac{{R^+}^2}{{R_T}^3 - {R^+}^3}. \tag{A.3}$$

Since $C(r)$ does not depend on time, this equation holds for any $r \leqslant R^+(t)$ (i.e. everywhere in the solid) and can be written as:

$$\frac{1}{C}\frac{\mathrm{d}C}{\mathrm{d}r} - \frac{1}{D}\frac{\mathrm{d}D}{\mathrm{d}r} = 3(1-D)\frac{r^2}{{R_T}^3 - r^3}. \tag{A.4}$$

Equation (A.4) is general and allows to take into account variations of D. However, it is useful to consider the limiting case of a constant partition coefficient D. In that case, a solution to this equation is

$$C = C_0 \left(\frac{{R_T}^3 - R^{-3}}{{R_T}^3 - r^3} \right)^{1-D}, \tag{A.5}$$

with $C_0 = DC_{l0}$ the mass fraction of FeO in the first solid formed.

Note that eq. (A.5) diverges when $r \to R_T$ but is in fact only valid as long as $C < 1$ and $C_l < 1$. When C_l reaches 1, the solid formed has the same composition as the liquid. The complete solution therefore is

$$C = \begin{cases} C_0 \left(\frac{{R_T}^3 - R^{-3}}{{R_T}^3 - r^3} \right)^{1-D} & \text{if } r < R_s \\ 1 & \text{if } r > R_s, \end{cases} \tag{A.6}$$

with

$$R_s = \left((R^-)^3 C_0^{\frac{1}{1-D}} + {R_T}^3 \left(1 - C_0^{\frac{1}{1-D}} \right) \right)^{1/3} \tag{A.7}$$

the value of $R^+(t)$ such that $C_l(t) = 1$.

B. Linear Stability

Since the solid is considered isoviscous and no source of toroidal flow is imposed at the boundaries, the velocity field can be expressed in terms of the scalar poloidal potential $\mathcal{P}$: $\mathbf{u} = \nabla \times \nabla \times (\mathcal{P}\mathbf{r})$ (e.g. Ricard and Vigny, 1989; Ribe, 2007). Linearizing eqs. (2.11) to (2.14) around the reference state $(\mathbf{u} = \mathbf{0}; \bar{T}; \bar{C})$ gives:

$$\mathcal{Q} = \nabla^2 \mathcal{P} \tag{B.1}$$

$$\nabla^2 \mathcal{Q} = \mathrm{Ra} \frac{\Theta - \langle \Theta \rangle}{r + \lambda} + \mathrm{Rc} \frac{c - \langle c \rangle}{r + \lambda} \tag{B.2}$$

$$\Gamma^2 \frac{\partial \Theta}{\partial t} + \frac{\partial \bar{T}}{\partial r} \frac{\mathcal{L}^2 \mathcal{P}}{r + \lambda} - \nabla^2 \Theta = W \left((r-1) \frac{\partial \Theta}{\partial r} + \left(\frac{\partial \bar{T}}{\partial r} \right)^+ \Theta \right) \tag{B.3}$$

$$\Gamma^2 \frac{\partial c}{\partial t} + \frac{\partial \bar{C}}{\partial r} \frac{\mathcal{L}^2 \mathcal{P}}{r + \lambda} = W(r-1) \frac{\partial c}{\partial r}. \tag{B.4}$$

The boundary conditions on the temperature and composition perturbations are trivial:

$$\Theta^{\pm} = 0, \tag{B.5}$$

$$c^{\pm} = 0. \tag{B.6}$$

The boundary condition eq. (2.16) and the free-slip boundary condition are written in term of the poloidal potential as:

$$\pm\Phi^{\pm}\frac{1}{r+\lambda}\mathcal{L}^2\mathcal{P}+\frac{\partial}{\partial r}\left(\frac{2}{r+\lambda}\mathcal{L}^2\mathcal{P}-(r+\lambda)\mathcal{Q}\right)=0 \tag{B.7}$$

$$\frac{\partial^2\mathcal{P}}{\partial r^2}+(\mathcal{L}^2-2)\frac{\mathcal{P}}{(r+\lambda)^2}=0. \tag{B.8}$$

$\lambda = R^-/L - 1$ is a curvature term due to the definition of the dimensionless radius. $\mathcal{L}^2$ is the horizontal laplacian: $\mathcal{L}^2\bullet = \partial_r((r+\lambda)^2\partial_r\bullet) - (r+\lambda)^2\nabla^2\bullet$. The quantity $\mathcal{Q}$ is introduced to ease the formulation of this system as an eigenvalue problem involving square matrices.

The perturbations $\mathcal{P}$, $\mathcal{Q}$, Θ and c are developed using spherical harmonics, e.g.

$$\mathcal{P}=\sum_{l=1}^{\infty}\sum_{m=-l}^{l}\mathcal{P}_l(r)Y_l^m(\theta,\phi)e^{\sigma_l t} \tag{B.9}$$

where l and m are the spherical harmonics degree and order and σ_l is the growth rate associated to the harmonic degree l. The system is laterally degenerated and m does not affect the growth rate of the perturbation nor the shape of the radial modes $\mathcal{P}_l(r)$, $\mathcal{Q}_l(r)$, $\Theta_l(r)$ and $c_l(r)$. These radial modes are discretized using a Chebyshev collocation approach (e.g. Guo et al., 2012; Canuto et al., 1985). Each radial mode is expressed as a vector whose components are the values at the $N+1$ Chebyshev nodal points (respectively denoted $\mathbf{P}$, $\mathbf{Q}$, $\mathbf{T}$ and $\mathbf{C}$). Radial derivatives evaluated at the nodal points $r_i = \frac{1}{2}\left(3+\cos\frac{i\pi}{N}\right)$ can then be expressed with a differentiation matrix $\mathbf{d}$, e.g. $\partial_r\mathcal{P}(r_i) = (\mathbf{dP})_i$. We formulate the system of linearized equations along with the associated boundary conditions as

$$\mathbf{LX}=\sigma_l\mathbf{RX} \tag{B.10}$$

with

$$\mathbf{X} = \begin{pmatrix} \mathbf{P} \\ \mathbf{Q} \\ \mathbf{T} \\ \mathbf{C} \end{pmatrix} \begin{matrix} 0:N \\ 0:N \\ 1:N-1 \\ 1:N-1 \end{matrix} \tag{B.11}$$

$$\mathbf{L} = \begin{array}{c} \begin{matrix} 0:N & 0:N & 1:N-1 & 1:N-1 \end{matrix} \\ \begin{pmatrix} \mathbf{d}^2 + (l_2-2)\underline{\mathbf{r}}_\lambda^{-2} & \mathbf{0} & \mathbf{0} & \mathbf{0} \\ \mathbf{D}^2 & -\mathbf{1} & \mathbf{0} & \mathbf{0} \\ \mathbf{d}^2 + (l_2-2)\underline{\mathbf{r}}_\lambda^{-2} & \mathbf{0} & \mathbf{0} & \mathbf{0} \\ l_2(\Phi^+\underline{\mathbf{r}}_\lambda^{-1} - 2\underline{\mathbf{r}}_\lambda^{-2} + 2\underline{\mathbf{r}}_\lambda^{-1}\mathbf{d}) & -(\mathbf{1}+\underline{\mathbf{r}}_\lambda\mathbf{d}) & \mathbf{0} & \mathbf{0} \\ \mathbf{0} & \mathbf{D}^2 & -\mathrm{Ra}\underline{\mathbf{r}}_\lambda^{-1} & -\mathrm{Rc}\underline{\mathbf{r}}_\lambda^{-1} \\ l_2(-\Phi^-\underline{\mathbf{r}}_\lambda^{-1} - 2\underline{\mathbf{r}}_\lambda^{-2} + 2\underline{\mathbf{r}}_\lambda^{-1}\mathbf{d}) & -(\mathbf{1}+\underline{\mathbf{r}}_\lambda\mathbf{d}) & \mathbf{0} & \mathbf{0} \\ -(\partial_r\bar{T})l_2\underline{\mathbf{r}}_\lambda^{-1} & \mathbf{0} & \mathbf{D}^2 + W^+\left((\underline{\mathbf{r}}-\mathbf{1})\mathbf{d} + (\partial_r\bar{T})^+\mathbf{1}\right) & \mathbf{0} \\ -(\partial_r\bar{C})l_2\underline{\mathbf{r}}_\lambda^{-1} & \mathbf{0} & \mathbf{0} & W^+(\underline{\mathbf{r}}-\mathbf{1})\mathbf{d} \end{pmatrix} \begin{matrix} 0 \\ 1:N-1 \\ N \\ 0 \\ 1:N-1 \\ N \\ 1:N-1 \\ 1:N-1 \end{matrix} \end{array} \tag{B.12}$$

$$\mathbf{R} = \begin{array}{c} \begin{matrix} 0:N & 0:N & 1:N-1 & 1:N-1 \end{matrix} \\ \begin{pmatrix} \mathbf{0} & \mathbf{0} & \mathbf{0} & \mathbf{0} \\ \mathbf{0} & \mathbf{0} & \mathbf{0} & \mathbf{0} \\ \mathbf{0} & \mathbf{0} & \Gamma^2\mathbf{1} & \mathbf{0} \\ \mathbf{0} & \mathbf{0} & \mathbf{0} & \Gamma^2\mathbf{1} \end{pmatrix} \begin{matrix} 0:N \\ 0:N \\ 1:N-1 \\ 1:N-1 \end{matrix} \end{array} \tag{B.13}$$

where $\mathbf{1}$ is the identity matrix, $\underline{\mathbf{r}}_{ij} = r_i\mathbf{1}_{ij}$, $\underline{\mathbf{r}}_\lambda = \underline{\mathbf{r}} + \lambda\mathbf{1}$, $l_2 = l(l+1)$ and $\mathbf{D}^2 = \mathbf{d}^2 + 2\underline{\mathbf{r}}_\lambda^{-1}\mathbf{d} - l_2\underline{\mathbf{r}}_\lambda^{-2}$ The extra row and column on top and right of the matrices are respectively the column and row indices of each of the submatrices. For example, the top left submatrix of the matrix $\mathbf{L}$ is only the first row (hence the 0 on the extra column) of the matrix $\mathbf{d}^2 + (l_2-2)\underline{\mathbf{r}}_\lambda^{-2}$.

At a given instant during the crystallization, all the dimensionless numbers W, λ, Γ, Ra and Rc appearing in the matrices $\mathbf{L}$ and $\mathbf{R}$ are known. For any harmonic degree l of the perturbation, finding its growth rate σ_l and associated vertical mode $\mathbf{X}$ is an eigenvalue problem. The largest eigenvalue is the growth rate, and the associated eigenvector represent the vertical modes. At a given instant, we look for the harmonic degree l with the highest growth rate σ_l, which is then used to compute the dimensional destabilization time scale $L_M^2/(\kappa\sigma)$.